Phased Array Radio Navigation System on UAVs: GNSS-based Calibration in the Field

Mika Okuhara, Torleiv Håland Bryne, Kristoffer Gryte, Tor Arne Johansen

Center for Autonomous Marine Operations and Systems, Department of Engineering Cybernetics
The Norwegian University of Science and Technology, Trondheim, Norway

Abstract— With global coverage, high accuracy, and lightweight receivers, global navigation satellite system (GNSS) has been the major positioning solution for unmanned aerial vehicles (UAV). However, GNSS is prone to electromagnetic interference and malicious attacks such as jamming or spoofing due to its low signal-to-noise ratio (SNR). To ensure the continuity and safety of UAV operation, the use of redundant navigation systems is crucial. Phased array radio system (PARS) has proven its potential as a local navigation solution in the last few years. PARS is robust against malicious attacks due to a significantly higher SNR than GNSS together with directional and encrypted transmission. One of the challenges of the PARS-based navigation is the radio antenna at ground station, as its orientation needs to be determined precisely to obtain accurate navigation solution for unmanned vehicles. This paper presents an automatic calibration algorithm for the ground radio antenna orientation using a multiplicative extended Kalman filter (MEKF) based on GNSS and PARS measurements. The calibration algorithm was tested with data obtained from a field test using a fixed wing UAV and validated by a residual analysis comparing the PARS- and GNSS-based positioning.

I. INTRODUCTION

Global navigation satellite systems (GNSS) have been the major solution for navigation systems of unmanned aerial vehicles (UAVs). This solution has some attractive features, like global coverage, lightweight receivers, high accuracy and low cost. However, GNSS is subject to jamming [1] and spoofing [2] due to its low signal-to-noise ratio (SNR). Additionally, a single error can decrease its performance or disable the positioning service. The use of a redundant positioning solution allows these issues to be overcome. For more frequent use of UAVs, especially in beyond line of sight (BLOS) flight, establishing a reliable alternative solution becomes more important.

In the past few years phased array radio system (PARS) has proven its potential on small UAVs [3]–[6]. Although PARS was primarily used as a high bandwidth radio communication link, it can also be used for positioning [4]. The strongly encrypted communication embedded in this system compensates the security issue of a GNSS solution, which is further mitigated by a much higher SNR. However, the drawback of PARS is that it requires radio line-of-sight and has lower accuracy than a GNSS solution [3]–[6].

Under the concern of cyber-security and with the need of a GNSS-free solution, PARS as a navigation system for small UAVs has been an ongoing research topic for a few years. At an earlier stage of a previous work, a nonlinear observer was used for PARS-aided inertial navigation system (INS) [4], and spoofing detection and mitigation in combination with GNSS- and PARS-aided INS [5]. In a more recent work, PARS-aided INS was implemented using multiplicative extended Kalman filter (MEKF) [7], [8]. The method was changed to MEKF as it can couple estimation errors between all states and apply the cross-covariance when fusing the INS-based estimation with PARS measurement as correction [6], [9].

A. Problem formulation and main idea

One of the critical points of PARS is that each time the ground radio antenna is moved, its full pose needs to be determined. This was done manually in the previous work, either by measuring the position and the attitude using a GNSS receiver and a compass, or by manually aligning PARS with the GNSS position. However, as the range from the ground radio becomes larger, a small error in antenna orientation induces large errors in measured PARS position. Thus, automatic estimation of the pose is an ideal method to achieve more accurate calibration results.

A similar problem setting can be seen in the area of vision-aided inertial navigation systems (V-INS's). The V-INS provides state estimates with combination of visual and inertial sensors. Its accuracy depends on a precise calibration of the rigid body transform between the sensors, and one of the major methods is a Kalman filter to estimate relative rotation and translation recursively [10]–[12]. Strapdown inertial navigation system (SINS) also uses a similar method. The SINS performance depends on the accuracy and speed of initial alignment process, which is one of the key technologies in SINS. The Kalman filer (KF) is widely used in the initial alignment [13] with the information from an external sensor device such as GNSS [14], odometer [15] and Doppler velocity log (DVL) [16]. Optimisation-based initial alignment is also suggested as obtaining a roughly known initial estimate required for KF is hard for an in-motion vehicle [17], [18]. However, as we are aiming to run the calibration algorithm online in parallel the system operation, and the PARS ground radio antenna orientation can be roughly estimated using a compass [6], and with more practical treatment of noise, Kalman filter is suitable for the antenna orientation calibration.

The main idea of this paper is to use GNSS data from the UAV for calibration of the antenna orientation. This assumes that GNSS is available during the initial phase of flight, near

the ground control station. After this initial calibration phase, navigation might proceed without GNSS, using PARS only. The accuracy of the calibration should benefit both from a long calibration period, and from a long range between the UAV and the ground station. If GNSS is not available during the initial flight, this method cannot be used, and less accurate PARS navigation must be accepted.

B. Main contribution

In this work, an automatic estimation of the PARS antenna orientation was implemented using MEKF. This filter fuses PARS and GNSS measurements and estimates the optimal antenna orientation. As PARS measurements of UAV flying over water contain outliers due to the radio reflection from the water surface, as seen in the past work [3]–[6], outlier rejection was also included.

C. Organization

This paper starts with mathematical preliminaries in Section II. Brief concepts of sensor suits for positioning are described in Section III. Section IV presents the basics of MEKF and explains how the calibration algorithm was implemented. Practical aspects of a test flight are then described in Section V and the results from the calibration MEKF are discussed in Section VI.

II. PRELIMINARIES

Before presenting PARS positioning and MEKF-based calibration, some mathematical preliminaries are stated in this section.

A. Notation

The Euclidean vector norm is denoted $\|\cdot\|_2$, and an identity matrix is denoted $\boldsymbol{I}$. The transpose of a vector or a matrix is denoted $(\cdot)^{\mathsf{T}}$. Coordinate frames are expressed as $\{\cdot\}$, while $\boldsymbol{z}_{bc}^a \in \mathbb{R}^3$ denotes a vector $\boldsymbol{z}$ from frame $\{b\}$ to $\{c\}$, resolved in $\{a\}$. $\boldsymbol{S}(\cdot) \in SS(3)$ denotes a skew symmetric matrix such that $\boldsymbol{S}(\boldsymbol{z}_1)\boldsymbol{z}_2 = \boldsymbol{z}_1 \times \boldsymbol{z}_2$ for two vectors $\boldsymbol{z}_1, \boldsymbol{z}_2 \in \mathbb{R}^3$. In addition, $\mathrm{diag}(\star_1, ..., \star_n)$ represents a diagonal matrix which places the n arguments diagonally, where $\star$ is a variable placeholder.

B. Attitude representations and relationships

The rotation vector

$$\boldsymbol{a}_\phi \equiv \phi\boldsymbol{e} \qquad (1)$$

is a general class of three-parameter attitude representations of a rigid body with one point fixed whose rotation is denoted by ϕ about some axis, which we specify by a unit vector $\boldsymbol{e}$.

In this paper, attitudes are represented in the unit quaternion, using the Hamiltonian representation. For rotations from some frame $\{a\}$ to another frame $\{b\}$, the unit quaternion is given as

$$\boldsymbol{q}_a^b = \begin{pmatrix} q_s \\ \boldsymbol{q}_v \end{pmatrix} = \begin{pmatrix} \cos(\frac{\phi}{2}) \\ \boldsymbol{e} \, \sin(\frac{\phi}{2}) \end{pmatrix}. \qquad (2)$$

The unit quaternion contains the *real* or *scalar* part referred as q_s, and the *imaginary* or *vector* part as $\boldsymbol{q}_v = (q_x, q_y, q_z)^{\mathsf{T}}$, which are related to the axis, $\boldsymbol{e}$ and angle of rotation, ϕ.

The rotation matrix, $\boldsymbol{R}_a^b \in SO(3)$, represents the rotation between $\{a\}$ and $\{b\}$ frames. The quaternion can be used to calculate rotation matrix, $\boldsymbol{R}_a^b \in SO(3)$,

$$\boldsymbol{R}_a^b(\boldsymbol{q}_a^b) = \left(q_s^2 - \boldsymbol{q}_v^{\mathsf{T}}\boldsymbol{q}_v\right)\boldsymbol{I}_3 + 2q_s\boldsymbol{S}(\boldsymbol{q}_v) + 2\boldsymbol{q}_v\boldsymbol{q}_v^{\mathsf{T}}, \qquad (3)$$

as in e.g. [8, Eq. (4)], [7, Eq. (117)] and [19, App. D.2].

The Hamiltonian quaternion product, denoted $\otimes$, is given such that

$$\boldsymbol{q}_3 = \boldsymbol{q}_1 \otimes \boldsymbol{q}_2 = \begin{pmatrix} q_{1_s}q_{2_s} - \boldsymbol{q}_{1_v}^{\mathsf{T}}\boldsymbol{q}_{2_v} \\ q_{1_s}\boldsymbol{q}_{2_v} + q_{2_s}\boldsymbol{q}_{1_v} + \boldsymbol{S}\left(\boldsymbol{q}_{1_v}\right)\boldsymbol{q}_{2_v} \end{pmatrix}, \qquad (4)$$

as in [7, Eq. (13)] and [19, App. D.2].

In this paper, the attitude error is denoted $\delta\boldsymbol{q}$ and relates to the true quaternion $\boldsymbol{q}$ by

$$\boldsymbol{q} = \hat{\boldsymbol{q}} \otimes \delta\boldsymbol{q}(\delta\boldsymbol{a}) \qquad (5)$$

where $\hat{\boldsymbol{q}}$ is the nominal estimated unit quaternion. The three dimensional attitude error, and state of the MEKF, $\delta\boldsymbol{a}$ is parameterized using four times the Modified Rodrigues Parameters (MRPs), $\delta\boldsymbol{p}$ related to $\delta\boldsymbol{q}$

$$\delta\boldsymbol{p} \equiv \frac{\delta\boldsymbol{q}_v}{1 + \delta q_s} = \boldsymbol{e}\tan\left(\frac{\phi}{4}\right) \equiv \frac{\delta\boldsymbol{a}}{4}, \qquad (6)$$

as given in [8, Eq. (10)]. The last two terms ensure that $a_p = \|\delta\boldsymbol{a}\|_2$ is approximately equal to ϕ for small rotations. As given in [8, Eq. (18c)], the error quaternion is calculated as

$$\delta\boldsymbol{q}(\delta\boldsymbol{a}) = \frac{1}{16 + a_p^2}\begin{pmatrix} 16 - a_p^2 \\ 8\delta\boldsymbol{a} \end{pmatrix}. \qquad (7)$$

Additionally, the Euler angles (roll, pitch and yaw) are represented as

$$\boldsymbol{\Theta} = \begin{pmatrix} \phi, & \theta, & \psi \end{pmatrix}^{\mathsf{T}}, \qquad (8)$$

and relate to rotation matrix using

$$\boldsymbol{R}(\Theta) = \begin{pmatrix} c\theta c\psi & -c\phi s\psi + s\phi s\theta c\psi & s\phi s\psi + c\phi s\theta c\psi \\ c\theta s\psi & c\phi c\psi + s\phi s\theta s\psi & -s\phi c\psi + c\phi s\theta s\psi \\ -s\theta & s\phi c\theta & c\phi c\theta \end{pmatrix} \qquad (9)$$

where $c\star$ denotes $\cos(\star)$ and $s\star$ denotes $\sin(\star)$.

C. Coordinate Frames

In this paper, four coordinate frames are considered. The first three are the Earth Centered Earth Fixed (ECEF) frame, an Earth-fixed North East Down (NED) frame and the BODY reference frame of the UAV, denoted $\{e\}$, $\{n\}$ and $\{b\}$ respectively, as indicated in Fig. 1. Although in other aerospace applications, the origin of an NED frame is usually on an aircraft, in this paper, the origin of the NED frame is located in the center of the PARS ground radio antenna. The forth coordinate frame is PARS coordinate frame, denoted $\{r\}$. The PARS coordinate system resembles the NED frame with coincided origins (i.e. $O_n = O_r$), however, rotated with respect to the NED frame, as indicated in Fig. 2.
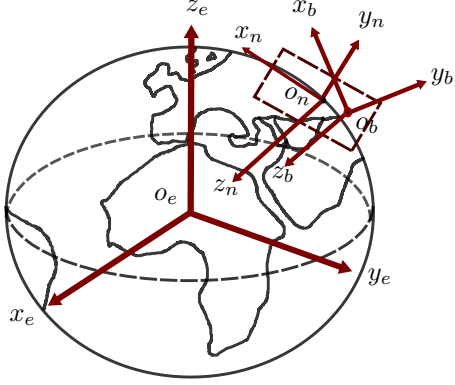
Fig. 1: Definitions of the ECEF, the NED and the BODY coordinate frames

Fig. 2: Range/azimuth/elevation measurements in PARS. ψ_r denotes the yaw angle between $\{n\}$ and $\{r\}$.

III. POSITIONING

A. Real-time kinematic GNSS

The real-time-kinematic (RTK) positioning is known as high accuracy GNSS. By performing relative positioning from a GNSS ground station with a known position to a rover by transmitting raw GNSS observable from the ground station to the rover, (UAV in this work), RTK achieves centimetre-level accuracy. RTK GNSS solution was used to provide ground truth of UAV position in this paper due to its high accuracy. The altitude measurement based on RTK GNSS was also used as a replacement of PARS vertical measurement as stated in Section III-C

B. Phased Array Radio System positioning

Although PARS' primary usage is communication, it can also be used as a positioning system as stated earlier.

The azimuth angle, ψ_u and elevation angle, θ_u of the UAV in the PARS coordinate frame, $\{r\}$ can be measured from the phase difference in incoming signals between the antenna elements of the ground radio. This is known as the direction-of-arrival (DOA) problem [20]–[22]. By accurately timing the transmission time of the signal, a measurement of the geometric range ρ_u between the PARS ground antenna to the UAV is found. A physical intuition of the range ρ_u, elevation angle θ_u and azimuth angle ψ_u in the $\{r\}$-frame can be seen in Fig. 2. With including zero-mean Gaussian noise $\varepsilon_\star \sim \mathcal{N}(0, \sigma_\star^2)$, actual measurements are represented as

$$\rho_m = \rho_u + \varepsilon_\rho, \tag{10}$$
$$\psi_m = \psi_u + \varepsilon_\psi, \tag{11}$$
$$\theta_m = \theta_u + \varepsilon_\theta. \tag{12}$$

The range ρ_u, azimuth ψ_u and elevation θ_u can be related to the UAV position in the radio coordinate system $\{r\}$ using

$$\boldsymbol{p}_{\text{PARS}}^r = \begin{pmatrix} p_{rb,x}^r \\ p_{rb,y}^r \\ p_{rb,z}^r \end{pmatrix} = \begin{pmatrix} \rho_u \cos(\psi_u) \cos(\theta_u) \\ \rho_u \sin(\psi_u) \cos(\theta_u) \\ -\rho_u \sin(\theta_u)) \end{pmatrix}, \tag{13}$$
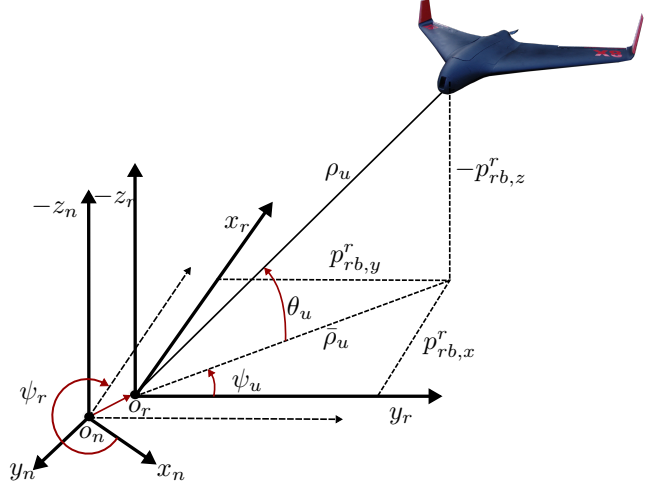
which is derivable from Fig. 2.

Following [23, Section 1.7.4], the bias arising from the nonlinear mapping of the azimuth and elevation angle measurement noise into Cartesian coordinates can be corrected by

$$\bar{\boldsymbol{p}}_{\text{PARS}}^r = \begin{pmatrix} b_\psi^{-1} b_\theta^{-1} \rho_m \cos(\psi_m) \cos(\theta_m) \\ b_\psi^{-1} b_\theta^{-1} \rho_m \sin(\psi_m) \cos(\theta_m) \\ -b_\theta^{-1} \rho_m \sin(\theta_m) \end{pmatrix}, \tag{14}$$

where $b_\psi = \mathbb{E}[\cos(\varepsilon_\psi)] = e^{-\sigma_\psi^2/2}$ and $b_\theta = \mathbb{E}[\cos(\varepsilon_\theta)] = e^{-\sigma_\theta^2/2}$. Based on (14), the PARS position can be converted from $\{r\}$ frame to $\{n\}$ frame using

$$\boldsymbol{p}_{\text{PARS}}^n = \boldsymbol{R}_r^n(\boldsymbol{q}_{\text{PARS}}) \bar{\boldsymbol{p}}_{\text{PARS}}^r, \tag{15}$$

where the unit quaternion $\boldsymbol{q}_{\text{PARS}} = \boldsymbol{q}_r^n$, represents the rotation from $\{r\}$ to $\{n\}$, to be obtained during the calibration of the mounting of the PARS ground antenna, which is the main aim of this paper.

C. PARS and GNSS positioning

As presented in [3], the PARS vertical measurement is sometimes very noisy as the elevation angle is prone to multipath errors due to the reflections from water surfaces. To avoid this issue, the vertical measurement in (13) was replaced by an altitude measurement based on RTK GNSS [1] $\gamma_{Alt,m} = p_{Alt,z}^r + \varepsilon_{Alt}$. The PARS range was also aided by RTK GNSS measurement to prevent the noise in elevation angle measurement from affecting the horizontal positioning

$$\bar{\rho}_m = \sqrt{\rho_m^2 - \gamma_{Alt,m}^2}, \tag{16}$$

[1] While RTK GNSS is used to provide the altitude during calibration, barometric sensor provides the replacement during system operation after calibration.

where $\bar{\rho}_m$ represents a measurement of the horizontal range. The resulting Cartesian position measurement becomes

$$p^r_{\text{PARS,Alt}} = \begin{pmatrix} \bar{\rho}_m \cos(\psi_m) \\ \bar{\rho}_m \sin(\psi_m) \\ -\gamma_{Alt,m} \end{pmatrix}. \qquad (17)$$

Furthermore, the covariance of the original PARS measurement ρ_m, ψ_m and $\gamma_{Alt,m}$ is

$$\mathcal{R}_{\text{PARS}} = \text{diag}(\mathbb{E}[\varepsilon_\rho^2], \mathbb{E}[\varepsilon_\psi^2], \mathbb{E}[\varepsilon_{Alt}^2]), \qquad (18)$$

and the covariance of $p^r_{\text{PARS,Alt}}$ can be computed using

$$\mathcal{R}^r_{PARS}(t) = M(t)\mathcal{R}_{\text{PARS}}M^{\mathsf{T}}(t). \qquad (19)$$

Here, $\mathcal{R}_{\text{PARS}}$ given in cylindrical coordinates is converted to $\mathcal{R}^r_{PARS}(t)$ in Cartesian coordinates [24, Ch. 1.6]. $M(t)$ is a Jacobian matrix of $p^r_{\text{PARS,Alt}}$ with respect to the noise $\varepsilon = (\varepsilon_\rho, \varepsilon_\psi, \varepsilon_{Alt})^{\mathsf{T}}$:

$$M = \frac{\partial p^r_{\text{PARS,Alt}}}{\partial \varepsilon} = \begin{pmatrix} m_{11} & m_{12} & m_{13} \\ m_{21} & m_{22} & m_{23} \\ 0 & 0 & 1 \end{pmatrix}, \qquad (20)$$

with

$$m_{11} = \frac{\cos(\psi_m)\rho_m}{\bar{\rho}_m} \qquad m_{12} = -\sin(\psi_m)\bar{\rho}_m$$

$$m_{13} = -\frac{\cos(\psi_m)\gamma_{Alt,m}}{\bar{\rho}_m} \qquad m_{21} = \frac{\sin(\psi_m)\rho_m}{\bar{\rho}_m}$$

$$m_{22} = \cos(\psi_m)\bar{\rho}_m \qquad m_{23} = -\frac{\sin(\psi_m)\gamma_{Alt,m}}{\bar{\rho}_m}.$$

In addition, the measurement in (17) $p^r_{\text{PARS,Alt}}$ and its covariance can be transformed from $\{r\}$ frame to $\{n\}$ frame by taking

$$p^n_{\text{PARS,Alt}} = R^n_r \, p^r_{\text{PARS,Alt}} \qquad (21)$$

$$\mathcal{R}^n_{PARS}(t) = R^n_r M(t)\mathcal{R}_{\text{PARS}}M^{\mathsf{T}}(t)R^{n\mathsf{T}}_r. \qquad (22)$$

IV. THE CALIBRATION ALGORITHM

The PARS antenna calibration problem is essentially to estimate the relative orientation of the PARS coordinate frame $\{r\}$ and the navigation frame $\{n\}$. The measurements available for this are the GNSS position of the UAV and the measurements of the PARS system (range and elevation and azimuth angles). In addition, the position of the PARS antenna is assumed to be known.

A. Multiplicative extended Kalman Filter

The main feature of Multiplicative extended Kalman filter (MEKF) is that it estimates the error between nominal state and true state instead of estimating a full state. The estimated error state δq^n_r is used as a correction to the nominal state $\hat{q}^n_r$ to get closer to the true state q^n_r, being a unit quaternion representing the rotation between the $\{r\}$ and the $\{n\}$:

$$q^n_r = \hat{q}^n_r \otimes \delta q^n_r(\delta a). \qquad (23)$$

Please note that the error state is computed in four times the MRPs δa other than rotation matrix or quaternion, and converted to δq^n_r when correcting the nominal state.

The MEKF at time $k + 1$ is computed in the following order:

1) Update nominal state with the constant orientation model

$$\hat{q}^n_r[k+1] = q^n_r[k] \qquad (24)$$

2) Propagate uncertainty

$$\hat{\mathcal{P}}[k+1] = \mathcal{P}[k] + \mathcal{Q}[k] \qquad (25)$$

3) If a measurement is available,
   a) Compute Kalman gain

$$K[k+1] = \hat{\mathcal{P}}[k+1]H^{\mathsf{T}}[k+1]$$
$$(H[k+1]\hat{\mathcal{P}}[k+1]H^{\mathsf{T}}[k+1] + \mathcal{R}[k+1])^{-1} \qquad (26)$$

   b) Compute error state

$$\delta a[k+1] = K[k+1](y[k+1] - h_{k+1}(\hat{q}^n_r[k+1], 0)) \qquad (27)$$

   c) Correct nominal state using (23)
   d) Correct state covariance

$$\mathcal{P}[k+1] = (I - K[k+1]H[k+1])\hat{\mathcal{P}}[k+1]$$
$$(I - K[k+1]H[k+1])^{\mathsf{T}}$$
$$+ K[k+1]\mathcal{R}[k+1]K[k+1]^{\mathsf{T}} \qquad (28)$$

Prediction step corresponds to 1) and 2), and correction step corresponds to 3). $\mathcal{Q}$ and $\mathcal{R}$ are from zero mean process noise $w \sim \mathcal{N}(0, \mathcal{Q})$ and measurement noise $v \sim \mathcal{N}(0, \mathcal{R})$. A measurement y, a nonlinear measurement function h_{k+1}, and a Jacobean matrix of h_{k+1} with respect to x, H are from a linearized measurement model

$$y[k+1] = \hat{y}[k+1] + H[k+1]\delta a[k+1], \qquad (29)$$

where $\hat{y}[k+1] = h_{k+1}(\hat{q}[k+1], 0)$.

B. Measurement model

The measurement model is formulated based on the following relationship between the UAV position (p^e_{eb}), the ground station position (p^e_{er}) and UAV PARS position relative to the ground radio (p^r_{rb}):

$$p^e_{eb} = p^e_{er} + R^e_n R^n_r p^r_{rb}. \qquad (30)$$

Firstly, moving p^e_{er} from RHS to LHS yields

$$p^e_{eb} - p^e_{er} = R^e_n R^n_r p^r_{rb}. \qquad (31)$$

By multiplying both sides by $R^{e\mathsf{T}}_n$ and using $R^n_r = \hat{R}^n_r(I_3 + S(\delta a))$,

$$R^{e\mathsf{T}}_n(p^e_{eb} - p^e_{er}) = R^{e\mathsf{T}}_n R^e_n R^n_r p^r_{rb} \qquad (32)$$
$$= \hat{R}^n_r(I_3 + S(\delta a))p^r_{rb} \qquad (33)$$
$$= \hat{R}^n_r p^r_{rb} + \hat{R}^n_r S(\delta a)p^r_{rb}. \qquad (34)$$

Swapping cross product between $\boldsymbol{p}_{rb}^r$ and $\delta\boldsymbol{a}$ yields

$$\underbrace{\boldsymbol{R}_n^{e\mathsf{T}}(\boldsymbol{p}_{eb}^e - \boldsymbol{p}_{er}^e)}_{\boldsymbol{y}} = \underbrace{\hat{\boldsymbol{R}}_r^n \boldsymbol{p}_{rb}^r}_{\hat{\boldsymbol{y}}} \underbrace{-\hat{\boldsymbol{R}}_r^n \boldsymbol{S}(\boldsymbol{p}_{rb}^r)}_{\boldsymbol{H}} \delta\boldsymbol{a}. \quad (35)$$

Comparing (35) and (29),

$$\boldsymbol{y} = \boldsymbol{R}_n^{e\mathsf{T}}(\boldsymbol{p}_{eb}^e - \boldsymbol{p}_{er}^e) \quad (36)$$

$$\hat{\boldsymbol{y}} = \hat{\boldsymbol{R}}_r^n \boldsymbol{p}_{rb}^r \quad (37)$$

$$\boldsymbol{H} = -\hat{\boldsymbol{R}}_r^n \boldsymbol{S}(\boldsymbol{p}_{rb}^r). \quad (38)$$

GNSS and PARS measurements correspond to $\boldsymbol{p}_{eb}^e$ and $\boldsymbol{p}_{rb}^r$ (i.e. $\boldsymbol{p}_{\mathrm{PARS,Alt}}^r$), respectively. $\boldsymbol{R}_n^{e\mathsf{T}}$ and $\boldsymbol{p}_{er}^e$ are considered to be known since these can be computed from the surveyed ground antenna location. These measurements are injected into the correction step (26)–(28), where $\boldsymbol{\mathcal{R}} = \boldsymbol{\mathcal{R}}_{\mathrm{RTK}}^n + \boldsymbol{\mathcal{R}}_{\mathrm{PARS}}^n$ is a sum of RTK and PARS measurement noise matrices, and where $\boldsymbol{\mathcal{R}}_{\mathrm{RTK}}^n = \boldsymbol{R}_n^{e\mathsf{T}} \boldsymbol{\mathcal{R}}_{\mathrm{RTK}}^e \boldsymbol{R}_n^e$.

C. Noise mitigation

To mitigate noise effects in PARS measurements, some practical modifications were made.

Firstly, as the elevation angles of PARS measurements are especially noisy, the PARS measurement equation was reformulated as described in Section III-C.

Secondly, as the PARS measurement, $\boldsymbol{p}_{rb}^r$ in the skew matrix of $\boldsymbol{H}$ was still noisy even though replacing the elevation angles by altitudes, $\boldsymbol{p}_{rb}^r$ was expressed by less noisy RTK measurement of UAV, $\boldsymbol{p}_{eb}^e$ and antenna locations, $\boldsymbol{p}_{er}^e$ by arranging (31),

$$\boldsymbol{p}_{rb}^r = \hat{\boldsymbol{R}}_r^{n\mathsf{T}} \boldsymbol{R}_n^{e\mathsf{T}}(\boldsymbol{p}_{eb}^e - \boldsymbol{p}_{er}^e) \quad (39)$$

and the equation (39) was substituted into the skew matrix of $\boldsymbol{H}$ in equation (38) to reduce the noise effect in the $\boldsymbol{H}$ matrix:

$$\boldsymbol{H} = -\hat{\boldsymbol{R}}_r^n \boldsymbol{S}(\hat{\boldsymbol{R}}_r^{n\mathsf{T}} \boldsymbol{R}_n^{e\mathsf{T}}(\boldsymbol{p}_{eb}^e - \boldsymbol{p}_{er}^e)). \quad (40)$$

Here, the risk of this modification is the nominal state of antenna orientation $\hat{\boldsymbol{R}}_r^n$. If this estimate is too far from the true state, this modification induces error in computation of $\boldsymbol{H}$ compared to using the measured $\boldsymbol{p}_{rb}^r$ vector.

D. Outlier rejection

As mentioned in Section I, the PARS measurements are sometimes very noisy due to reflections from water surface. Outlier rejection was implemented to prevent bad PARS measurements from degrading the estimation. If the test statistic

$$T(\boldsymbol{y}) = (\boldsymbol{y} - \hat{\boldsymbol{y}})^\mathsf{T}(\boldsymbol{H}\hat{\boldsymbol{P}}\boldsymbol{H}^\mathsf{T} + \boldsymbol{V})^{-1}(\boldsymbol{y} - \hat{\boldsymbol{y}}) \sim \chi_1^2 \quad (41)$$

is above some limit χ_α^2, the measurement is discarded as outlier [25, Section 7.6.1].

E. Validation

The estimated antenna orientation is validated by evaluating the residual between PARS and RTK GNSS measurements,

$$\boldsymbol{p}_{nb\mathrm{PARS}}^n - \boldsymbol{p}_{nb\mathrm{RTK}}^n. \quad (42)$$

The RTK GNSS measurement in $\{n\}$ frame was computed as[2]

$$\boldsymbol{p}_{nb\mathrm{RTK}}^n = \boldsymbol{R}_e^n(\boldsymbol{p}_{eb}^e - \boldsymbol{p}_{er}^e), \quad (43)$$

and the position based on PARS measurements in $\{n\}$ frame was calculated using[3]

$$\boldsymbol{p}_{nbPARS}^n = \boldsymbol{R}_r^{n*} \boldsymbol{p}_{rb}^r, \quad (44)$$

where

$$\boldsymbol{R}_r^{n*} = \begin{pmatrix} r_{11} & r_{12} & 0 \\ r_{21} & r_{22} & 0 \\ 0 & 0 & 1 \end{pmatrix}, \quad (45)$$

whereas r_{11}–r_{22} are elements taken from the estimated matrix $\boldsymbol{R}_r^n$.

$\boldsymbol{R}_r^n$ was modified as RTK GNSS altitude was used instead of PARS elevation angle. This modification might induce some biases in x- and y-components of $\boldsymbol{p}_{nbPARS}^n$, since the effect of non-zero roll and pitch angles were ignored. If the roll and pitch angles are zero and only yaw angle affects the rotation between $\{r\}$ frame and $\{n\}$ frame, the z-component of $\boldsymbol{p}_{nb}^r$ does not affect x- and y-components. However, when the roll and pitch angles are not exactly zero, the contribution of the z-component has an effect.

V. PRACTICAL ASPECTS

A field test was carried out on October 8th 2020 in good weather conditions at the north of Agdenes outside of Trondheim, Norway. Multiple flights with a Skywalker X8 UAV were performed. The tracks of the first and second UAV flights, named "flight 1" and "flight 2", are given in Fig. 3. A system overview of the hardware used in this field test is given in Fig. 4.

A. Payload

The avionics of the UAV contained a Pixhawk autopilot running ArduPlane flight control software with a GNSS, Honeywell HMC5883L 3-axis digital compass IC, MS5611-01BA03 barometric pressure sensor and an internal IMU/INS.

In addition to the Pixhawk autopilot, the payload was also equipped with a tactical grade IMU[4], the Sensonor STIM 300 , and a Ublox F9P-ZED GNSS receiver to provide accurate RTK GNSS measurements, used as a ground truth to correct the PARS-based position estimates. To synchronize the timestamps of the IMU and GNSS measurements, a SenTiBoard [26] was used. This synchronization can ease

---

[2]$\boldsymbol{p}_{er}^e = \boldsymbol{p}_{en}^e$ since the origins of $\{n\}$ frame and $\{r\}$ frame coincide
[3]$\boldsymbol{p}_{nb}^r = \boldsymbol{p}_{rb}^r$ since the origins of $\{n\}$ frame and $\{r\}$ frame coincide
[4]Although IMU measurements were not used in this paper, STIM 300 was also mounted for future work.

the integration of the measurements to an Odroid XU4 on-board computer.

Furthermore, the Radionor Communications CRE2 144-LW PARS was used to send telemetry data to the ground station and to receive commands and PARS measurements. To satisfy the redundancy requirements of beyond visual-line-of-sight flight, a 433 MHz 3DR radio was used as a redundant telemetry link. References [5], [9] provide further details about the payload.

B. Ground station

A ground station was set up to compute RTK GNSS data and PARS positioning data and to pilot a UAV. The ground station consisted of a laptop computer, a uBlox F9P-ZED GNSS receiver, and a Radionor Communications CRE2-189 PARS. The CRE2-189 is a ground radio which contains an array of 8x8 antenna elements. The PARS was set to a 2 Mbit/s mode with a maximal distance of up to 60 km.

Fig. 3: Flight paths of the UAV based on RTK GNSS (yellow—flight 1, red—flight 2)

C. Initial calibration

The PARS provides a position measurement in local radio frame $\{r\}$. Therefore, pre-flight calibration to obtain the ground radio orientation is essential for accurate position estimates. As the algorithm shown in the Section IV requires reasonably accurate initial estimates, the antenna orientation angles were measured using a compass. However, the compass gave only a crudely known angle as the compass measurement changes when it is close to a metal antenna. While the full orientation consists of the roll, pitch and yaw angles, only the yaw angle was measured, since the roll and pitch angles are close enough to zero, and were considered to be reasonable for the initial estimates. The PARS ground antenna position was identified using a GNSS receiver.

VI. RESULTS AND DISCUSSION

Offline calculations were carried out using the data obtained from the field test to verify the calibration algorithm presented in Section IV. The calibration algorithm was applied to the data from flight 1 and flight 2 with an identical ground antenna position and the results were compared
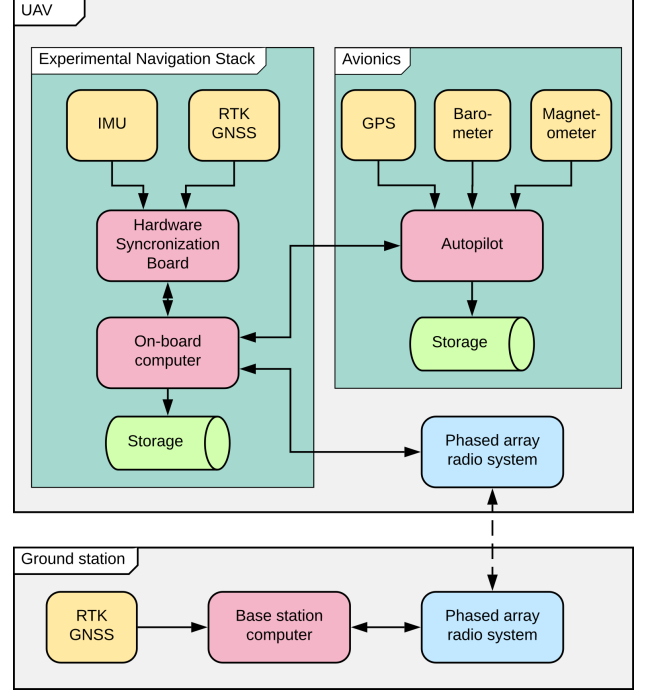

Fig. 4: System overview

between the two flights. In the offline calculations, rough estimates of the antenna orientation measured by a compass were used as an initial state:

$$\boldsymbol{\Theta}_{\mathrm{PARS}} = (\phi_r\,,\theta_r\,,\psi_r) = (0\,,0\,,-65.5°).$$

The initial $\boldsymbol{P}$, $\boldsymbol{Q}$, and $\boldsymbol{R}_\star$ matrices were set as follows:

$$\boldsymbol{P}_0 = \mathrm{diag}((3°)^2, (3°)^2, (50°)^2)$$
$$\boldsymbol{Q} = 0$$
$$\boldsymbol{R}_{\mathrm{PARS}} = \mathrm{diag}((15\,\mathrm{m})^2, (2°)^2, (5\,\mathrm{m})^2)$$
$$\boldsymbol{R}_{\mathrm{RTK}} = \mathrm{diag}((0.2\,\mathrm{m})^2, (0.2\,\mathrm{m})^2, (0.4\,\mathrm{m})^2).$$

$\boldsymbol{Q}$ was set to 0, as the ground antenna is stationary. The $\chi^2_\alpha = 7.815$ was chosen as the outlier rejection threshold.

Figure 5 shows the antenna orientation estimates from flight 1 and flight 2 in Euler angles. In addition to the compass measurement, extreme initial conditions were also considered by setting the initial yaw angle to $-52°$ and $-97°$. Even though the initial estimates contain a relatively large variance, both $\psi_r = -52°$ and $\psi_r = -97°$ cases converged.

In the situation when GNSS is not available initially but available only a short period at some point, it corrects the estimation fairly quickly, as Fig. 6 shows. Here, $1\,\mathrm{min}$ of RTK GNSS was made available for correction at mid-point in flight 2. Comparing with Fig. 5, applying calibration when the UAV is further might require shorter GNSS flight duration.

Table I shows the Euler angle estimates averaged over the last 100 iterations when $\psi_r = -65.5°$. Pitch gave the minimum and yaw gave maximum variance, since the PARS

measurements have better accuracy in range and elevation than azimuth due to the aid of RTK GNSS altitude. The difference in yaw angles between flight 1 and flight 2 was $0.144\,50°$ which gives $7.6164\,\text{m}$ error at the furthest point where the maximum ranges for flight 1 and flight 2 were 3.0225km and 3.0263km.

Table II shows the Euler angles averaged over last 100 iterations and means of residuals in flight 2 when $\psi_r = -65.5°$, where the antenna position has an error of 0.1m, 1m, and 10m. As the error becomes bigger, the induced errors in estimation increase. However, it still converges and gives relatively reasonable estimations even when the position error is 10m.

The estimated antenna orientation when $\psi_r = -65.5°$ was validated by the residual between the calibrated PARS and RTK GNSS measurements, as shown in Fig. 7. Apart from small biases due to (44), the residual gave reasonable results, which indicates that the estimated antenna orientation is promising.

	Flight 1	Flight 2
Roll [°]	0.0042313	0.0039529
Pitch [°]	-0.0014450	-0.0013951
Yaw [°]	-74.592	-74.736

TABLE I: Estimated antenna orientation in Euler angles

| Errors	0.1 m	1 m	10 m
Roll [°]	0.0037511	0.0019389	-0.015739
Pitch [°]	-0.0026741	-0.014184	-0.12920
Yaw [°]	-74.733	-74.702	-74.396
x [m]	0.64061	1.5273	10.362
y [m]	1.9636	2.2236	4.8465

TABLE II: Sensitivity of PARS antenna position in flight 2

VII. CONCLUSION

In this paper, an MEKF-based calibration algorithm which automatically estimates ground antenna orientation for phased array radio system (PARS) was implemented. The calibration algorithm was applied to data obtained from a field test which involves multiple flights with an identical position of a ground antenna. The antenna orientations estimated from two independent flights coincided and the suggested algorithm was proved to be robust and able to calibrate the antenna orientation based on RTK GNSS measurements. As future work, calibration using INS or additional PARS instead of GNSS is in the interest to achieve fully GNSS-free navigation system.

ACKNOWLEDGEMENTS
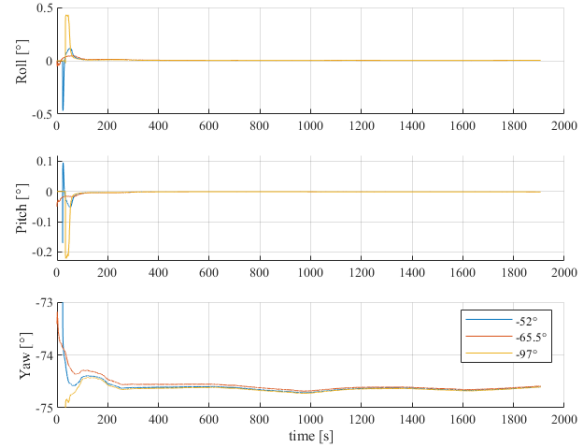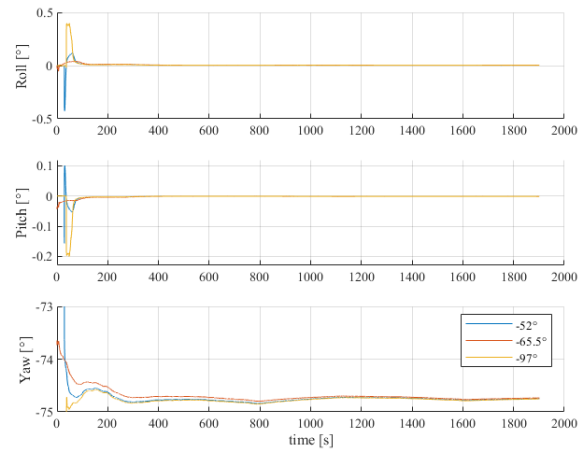
(a) flight 1

(b) flight 2

Fig. 5: Euler angles of antenna orientations

REFERENCES

[1] A. Pinker and C. Smith, "Vulnerability of the GPS signal to jamming," *GPS Solutions*, vol. 3, no. 2, pp. 19–27, 1999.

[2] A. J. Kerns, D. P. Shepard, J. A. Bhatti, and T. E. Humphreys, "Unmanned aircraft capture and control via GPS spoofing," *Journal of Field Robotics*, vol. 31, no. 4, pp. 617–636, 2014.

[3] S. M. Albrektsen, A Sægrov, and T. A. Johansen, "Navigation of uav using phased array radio," in *Workshop on Research, Education and Development of Unmanned Aerial Systems (RED UAS)*, 2017, pp. 138–143.
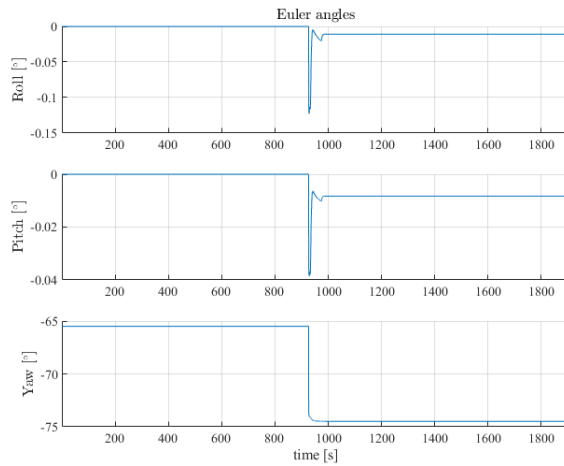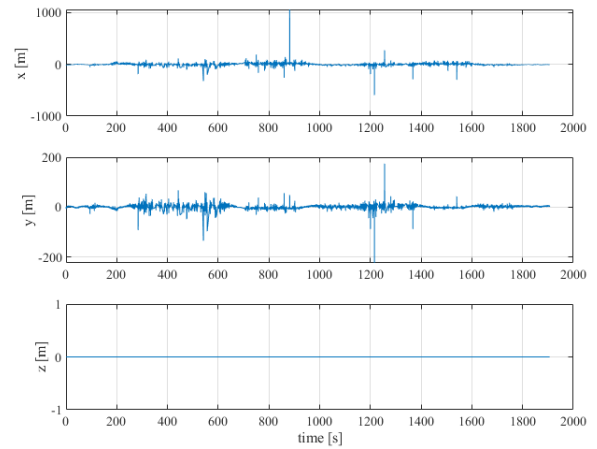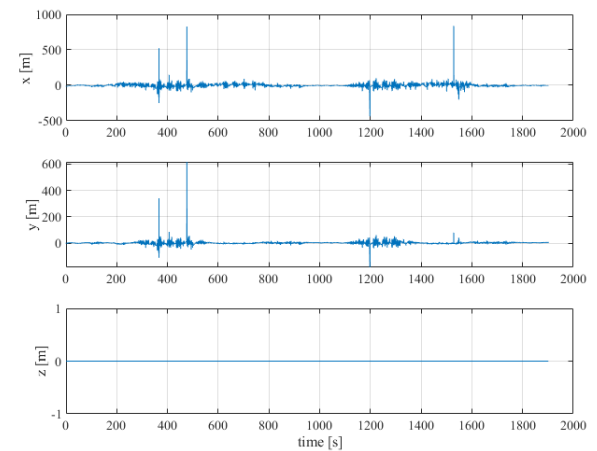
Fig. 6: Euler angles of antenna orientation in flight 2 when GNSS is available only 1 min

(a) flight 1

(b) flight 2

Fig. 7: Residual between calibrated PARS and RTK GNSS

[4] S. M. Albrektsen, T. H. Bryne, and T. A. Johansen, "Phased array radio system aided inertial navigation for unmanned aerial vehicles," in *Proc. of the IEEE Aerospace Conference*, Big Sky, Montana, 2018, pp. 1–11.

[5] ——, "Robust and secure uav navigation using gnss, phased-array radiosystem and inertial sensor fusion," in *2nd IEEE Conference on Control Technology and Applications*, Copenhagen, Denmark, 2018, pp. 1338–1345.

[6] K. Gryte, T. H. Bryne, S. M. Albrektsen, and T. A. Johansen, "Field test results of gnss-denied inertial navigation aided by phased-array radio systems for uavs," in *2019 International Conference on Unmanned Aircraft Systems (ICUAS)*, 2019, pp. 1398–1406.

[7] J. Solà, *Quaternion kinematics for the error-state kalman filter*, 2017.

[8] F. L. Markley, "Attitude error representation for kalman filtering," *Journal of Guidance, Control, and Dynamics*, vol. 26, no. 2, pp. 311–317, Mar. 2003.

[9] K Gryte, T. H. Bryne, and T. A. Johansen, "Unmanned aircraft flight control aided by phased-array radio navigation," *Journal of Field Robotics*, pp. 1–20, Dec. 2020.

[10] F. M. Mirzaei and S. I. Roumeliotis, "A kalman filter-based algorithm for imu-camera calibration: Observability analysis and performance evaluation," *IEEE Transactions on Robotics*, vol. 24, no. 5, pp. 1143–1156, 2008.

[11] J. Kelly and G. Sukhatme, "Visual-inertial sensor fusion: Localization, mapping and sensor-to-sensor self-calibration," *I. J. Robotic Res.*, vol. 30, pp. 56–79, Jan. 2011.

[12] M. Bloesch, M. Burri, S. Omari, M. Hutter, and R. Siegwart, "Iterated extended kalman filter based visual-inertial odometry using direct photometric feed-

back," *The International Journal of Robotics Research*, vol. 36, no. 10, pp. 1053–1072, 2017.

[13] G. Chang, "Fast two-position initial alignment for sins using velocity plus angular rate measurements," *Advances in Space Research*, vol. 56, no. 7, pp. 1331–1342, 2015.

[14] J. Liu and T. Zhao, "In-flight alignment method of navigation system based on microelectromechanical systems sensor measurement," *International Journal of Distributed Sensor Networks*, vol. 15, no. 4, 2019.

[15] J. Lu, C. Lei, Y. Yang, and M. Liu, "In-motion initial alignment and positioning with ins/cns/odo integrated navigation system for lunar rovers," *Advances in Space Research*, vol. 59, no. 12, pp. 3070–3079, 2017.

[16] W. Li, W. Wu, J. Wang, and M. Wu, "A novel backtracking navigation scheme for autonomous underwater vehicles," *Measurement*, vol. 47, pp. 496–504, 2014.

[17] K. Gao, S. Ren, X. Chen, and Z. Wang, "An optimization-based initial alignment and calibration

algorithm of land-vehicle sins in-motion," *Sensors*, vol. 18, no. 7, p. 2081, Jun. 2018.

[18] Z. Lu, J. Li, X. Zhang, K. Feng, X. Wei, D. Zhang, J. Mi, and Y. Liu, "A new in-flight alignment method with an application to the low-cost sins/gps integrated navigation system," *Sensors*, vol. 20, no. 2, p. 512, Jan. 2020.

[19] J. A. Farrell, *Aided Navigation: GPS with High Rate Sensors*. McGraw-Hill, 2008.

[20] H. Krim and M. Viberg, "Two decades of array signal processing research: The parametric approach," *IEEE Signal Processing Magazine*, vol. 13, no. 4, pp. 67–94, Jul. 1996.

[21] R. Roy and T. Kailath, "ESPRIT-estimation of signal parameters via rotational invariance techniques," *IEEE Transactions on Acoustics, Speech, and Signal Processing*, vol. 37, no. 7, pp. 984–995, 1989.

[22] R. Schmidt, "Multiple emitter location and signal parameter estimation," *IEEE Transactions on Antennas and Propagation*, vol. 34, no. 3, pp. 276–280, Mar. 1986.

[23] Y. Bar-Shalom, P. K. Willett, and X. Tian, *Tracking and Data Fusion: A Handbook of Algorithms*. YBS Publishing, 2011.

[24] Y. Bar-Shalom and X.-R. Li, *Multitarget-Multisensor Tracking: Principles and Techniques*. YBS Publishing, 1995.

[25] F. Gustafsson, *Statistical Sensor Fusion*, 2nd. Studentlitteratur, 2012.

[26] M. S. Albrektsen and T. A. Johansen, "User-configurable timing and navigation for UAVs," *Sensors*, vol. 18, no. 8, pp. 1–27, 2018.